Estimation of scattering properties modifications caused by in vivo human skin optical clearing using line-field confocal optical coherence tomography

Sergey M Zaytsev, Léna Waszczuk, Jonas Ogien, Arnaud Dubois, Walter Blondel, Marine Amouroux

Journal of Biophotonics

JOURNAL OF BIOPHOTONICS

RESEARCH ARTICLE OPEN ACCESS

Estimation of Scattering Properties Modifications Caused by In Vivo Human Skin Optical Clearing Using Line-Field Confocal Optical Coherence Tomography

Sergey M. Zaytsev[1] | Léna Waszczuk[2,3] | Jonas Ogien[3] | Arnaud Dubois[2,3] | Walter Blondel[1] | Marine Amouroux[1]

[1]Université de Lorraine, CNRS, CRAN UMR 7039, Vandoeuvre-lès-Nancy, France | [2]Université Paris-Saclay, Institut d'Optique Graduate School, CNRS, Laboratoire Charles Fabry, Palaiseau, France | [3]DAMAE Medical, Paris, France

Correspondence: Marine Amouroux (marine.amouroux@univ-lorraine.fr)

Received: 14 June 2024 | **Revised:** 18 September 2024 | **Accepted:** 9 October 2024

Funding: This work was supported by European Regional Development Fund, Contrat de Plan Etat-Région Grand Est 2015-2020, Agence Nationale de la Recherche, Ligue Contre le Cancer, Conseil régional du Grand Est.

Keywords: modeling | optical clearing | optical coherence tomography | optical properties | scattering | skin

ABSTRACT

The image contrast and probing depth of optical methods applied to in vivo skin could be improved by reducing skin scattering using the optical clearing method. The aim of this study was to quantify, from line-field confocal optical coherence tomography (LC-OCT) 3D images, the modifications of skin scattering properties in vivo during optical clearing. Nine mixtures of optical clearing agents were used in combination with physical and chemical permeation enhancers on the human skin of three healthy volunteers. Scattering coefficient and anisotropy factor of the epidermis and the upper dermis were estimated from the 3D LC-OCT images of skin using an exponential decay model of the in-depth intensity profile. We were able to demonstrate a decrease in epidermal scattering (down to 33%) related to optical clearing, with the best results obtained by a mixture of polyethylene glycol, oleic acid, and propylene glycol.

1 | Introduction

Human skin is an inhomogeneous organ comprised of three main layers: epidermis, dermis, and adipose tissue. Each of these layers differs in thickness and morphology. Playing a role of an interface between the body and the environment, the skin performs physiological barrier function, protecting the body from ultraviolet rays and external physical impact and retaining water inside the body [1]. Since the skin is actively exposed to external irritants, it is susceptible to various pathological processes that can affect different layers of the skin, depending on the type and stage of the lesion. Due to the importance of the skin for the proper functioning of the body, the noninvasive diagnosis of skin diseases is an extremely important task to which many studies are devoted. Optical methods based on the interaction of light with biological tissues have become a good potential addition or replacement to existing invasive methods (such as histopathological studies) due to their noninvasiveness, high sensitivity, the ability to obtain information in real time (without time-consuming preparation of histological samples), as well as potential for clinical implementation [2, 3].

Line-field confocal optical coherence tomography (LC-OCT) is a recently developed optical imaging method that combines the advantages of OCT and confocal microscopy, providing three-dimensional (3D) images of tissue with a quasi-isotropic resolution of ~1 μm that is high enough to distinguish the cellular skin structure [4, 5]. The applicability of LC-OCT to the diagnosis of skin

Abbreviations: CPE, chemical permeation enhancer; DMSO, dimethyl sulfoxide; LC-OCT, Line-field Optical Coherence Tomography; OA, oleic acid; OC, optical clearing; OCA, optical clearing agent; OCT, Optical Coherence Tomography; PEG, polyethylene glycol; PG, propylene glycol; RI, refractive index; SC, stratum corneum.

diseases (including skin cancers) has been widely demonstrated [6–8]. Besides information on tissue morphology, the LC-OCT images also contain information on tissue optical properties (OPs). Since LC-OCT is an interferometric method, the image is obtained by registering low-coherence light backscattered or reflected by the tissue. This signal depends on three main OPs of the imaged tissue: absorption $\mu_a(\lambda)$ and scattering $\mu_s(\lambda)$ coefficients, which determine the fraction of light absorbed or scattered over a unit path length, respectively, and the anisotropy factor $g(\lambda)$ that is the mean cosine of scattering angles along the photon trajectory. The in-depth LC-OCT image intensity $I(z)$ depends on these OPs and usually can be described (although only partially since the anisotropy, for example, is not taken into account) by a Beer–Lambert law in the single-scattering regime:

$$I(z) \propto exp^{-2\mu_t(\lambda)z}, \quad (1)$$

where z is depth in mm and $\mu_t(\lambda)=\mu_s(\lambda)+\mu_a(\lambda)$ is the total attenuation coefficient of the medium in mm^{-1} [9]. Those properties are determined by the size, density, and shape of the tissue constituents (cells, collagen, and elastin fibers, etc.). Assessing the OPs of skin is critical for tissue characterization and quantification of structural changes associated with the pathological process.

The method most widely reported in the literature for extracting $\mu_t(\lambda)$ with conventional OCT techniques is to fit an exponential decay curve to the depth-dependent average intensity profile [10]. However, only few works were dedicated to separate assessment of scattering, absorption, and anisotropy from OCT images [11]. Such an assessment may allow one to obtain more comprehensive quantitative information about structural changes induced by a particular process in the skin than when estimating the integral $\mu_t(\lambda)$ coefficient. However, this approach becomes complicated to implement when it comes to multilayered samples due to conventional OCT features and the concept of backscattered light as a fixed fraction of the attenuated light (which is assumed when extracting $\mu_t(\lambda)$ coefficient) [12]. In contrast, a model based on Monte-Carlo simulations developed by Jacques et al. [13] allows for a simple extraction of $\mu_s(\lambda)$ and $g(\lambda)$ from focus-tracking OCT techniques and confocal microscopy. This model was validated on phantoms with pre-defined OPs [14] and later applied to skin [15]. Since LC-OCT is a combination of OCT and confocal microscopy techniques, this technique is suitable for the application of the aforementioned model. In her work, Waszczuk et al. [16] demonstrated that, with preliminary calibration using a phantom with known OPs, it is possible to extract skin $\mu_s(\lambda)$ and $g(\lambda)$ OPs from 3D LC-OCT images of monolayered and bilayered phantoms.

However, the use of OCT (as well as other optical methods) for skin diagnosis is limited by strong light scattering in biological tissues, for example, in skin. Scattering reduces the image contrast and resolution, lowering the possible diagnostic potential of such methods. This scattering originates from the inhomogeneities of skin layers (intralayer and interlayer inhomogeneities), leading to a mismatch in refractive indices (RIs) between the tissue constituents and the interstitial fluid. To overcome this limitation, a tissue optical clearing (OC) method was proposed, based on the use of osmotic chemicals called optical clearing agents (OCAs), whose RI was close to that of tissue solid material [17, 18]. Being usually topically applied (but also can be injected into the tissue), OCA causes skin dehydration, which in some cases might be followed by replacement of the interstitial fluid with OCA and reversible collagen dissociation. All these effects (or only part of them, depending on the intensity of optical clearing) lead to the reduced scattering of treated tissue, leading to increased imaging depth and contrast [19].

Translation of skin OC into clinical use, however, is connected with the need to comply with established regulations on the use of drugs, especially if the possible application will be performed on a lesional tissue. Since OCA have been reported to have undesired side effects in vivo at pure concentrations [20, 21], their concentrations must be reduced in order to pass the threshold for clinical admission and biocompatibility [22]. However, the low concentration of OCA does not allow it to reach a sufficient clearing effect. To compensate for lower OCA concentrations in biocompatible applications, they can be used in conjunction with so-called chemical permeation enhancers (CPEs), which are chemicals capable of temporarily disrupting skin barrier functions. The chemicals most commonly used as CPEs are alcohols [23], dimethyl sulfoxide (DMSO), and fatty acids (oleic acid (OA)) [24]. There is also a large number of physical methods to enhance the skin permeability for OCA, such as microdermabrasion and therapeutic ultrasound [25], which can be combined with CPE for a more efficient biocompatible effect of OCA.

Such possibility of in vivo clearing of human skin using biocompatible OCA concentrations has been addressed in our previous study [26], where nine mixtures of one of three OCA compounds (polyethylene glycol (PEG), sucrose, and glucose water solutions) in combination with one of three CPE compounds (propylene glycol (PG), DMSO, and OA) were used with skin microdermabrasion and ultrasound to test their effectiveness in increasing LC-OCT in-depth image intensity and contrast. We thus demonstrated the potential of clinical use-compatible physical enhancers and OCA (concentrations and types) for optical clearing of human skin in vivo. The latter results were obtained by the analysis of LC-OCT 3D image intensity and contrast ratio modifications throughout the skin tissue depth; hence, the related changes in skin OPs were only "hypothesized." Consequently, the aim of this study was to effectively assess this OC-related modifications in skin OP by extracting (from the LC-OCT images) and analyzing quantitative estimates of skin epidermis and dermis scattering coefficients and anisotropy factors.

2 | Materials and Methods

In this study, the composition of OCA compounds, the skin sites under investigation, and the imaging modality were similar to our previously published work, where some complementary information could be found [26].

2.1 | OCAs and Permeability Enhancers

The choice of chemicals for this study was based on literature data on OCA currently used for human skin OC experiments [17]. Three chemicals from alcohol and sugar groups were used

as OCA compounds: polyethylene glycol—400 (PEG, Sigma-Aldrich, USA), 3 M aqueous solutions of Sucrose (Sigma-Aldrich, USA), and glucose (Sigma-Aldrich, USA). In order to satisfy the possible clinical admission requirements, OCA compounds did not exceed the threshold of a concentration for topical application in the form of a solution, established by FDA. Thus, the data from FDA inactive ingredients database were used to fix the concentration of OCA mixture compounds, mentioned hereafter [22]. As there was no information about the maximum concentration for glucose and sucrose solutions, a value (v/v) of 50% was established for this study as it was previously reported as the most efficient one for OCT-assessed optical clearing [27]. To increase the in vivo efficiency of reduced concentrations of OCA compounds, they were mixed with three compounds with permeation-enhancing properties (CPEs) from various chemical groups, such as alcohols, organic solvents, and fatty acids: PG (Sigma-Aldrich, USA), DMSO (Sigma-Aldrich, USA) and OA (Sigma-Aldrich, USA). Nine resulting mixtures of OCA and CPE and their corresponding compound concentrations are presented in Table 1. If it was not possible to mix OCA and CPE compounds only without exceeding FDA concentration thresholds, either complementary amount of distilled water or second CPE (namely PG) was added to the mixture. Additional information (such as the concentration threshold of each chemical used) can be found in our previous study [26].

2.2 | Technical Equipment

2.2.1 | LC-OCT

Detailed information on the LC-OCT device (DeepLive; DAMAE Medical, France) used for image acquisition in this study can be found in [28]. Briefly, it is a Linnik interferometer-based imaging system with line illumination by supercontinuum laser at a central wavelength of around 800 nm. A water-immersion microscope objective with a numerical aperture NA = 0.5 is incorporated in each arm of the interferometer. Backscattered spatially coherent light is detected using a line camera. By in-depth scanning (along z-axis) during the acquisition of horizontal section images with a field of view of 1.2 mm × 0.5 mm ($x \times y$), a stack of images can be compiled to obtain a 3D image of the tissue in situ with axial and lateral resolutions of less than 1.3 μm and a maximum penetration depth (z) of about 500 μm.

2.2.2 | Physical Permeability Enhancers

Therapeutic ultrasound (Pulson 100, Gymna, Belgium) was used as a physical permeability enhancer as it increases the skin permeability for OCA [25]. The duty cycle was 100%, the frequency 1 MHz, and the power density 1 W/cm^2. Also, the skin microdermabrasion device (Philips VisaCare, Philips, Netherlands) was used. This procedure is commonly applied in cosmetology and involves the abrasion of stratum corneum (SC) layer, leading to increased penetration rate of OCA into the skin.

2.3 | In Vivo Human Skin Sites

The experimental skin sites were the left- and right-hand thenar space dorsum of three healthy volunteers aged around 28 years with skin phototypes 2 and 3. An informed consent was obtained from the volunteers for topical OCA application, dermabrasion, and sonophoretic treatment of experimental skin sites and the acquisition of 3D LC-OCT images. Volunteers' safety was guaranteed by FDA-approved concentrations of OCAs and by CE-marked LC-OCT, dermabrasion, and sonophoresis medical devices. Since the dataset used in a current study had been acquired for the previously performed research [26], an authorization for the human skin studies in vivo was obtained from the Saratov State Medical University Ethical committee (protocol №11 by June 7th 2022).

2.4 | Optical Clearing Protocol

Ethanol-cleaned skin sites were subject to intact skin LC-OCT image acquisitions (t = 0 min). Then, after 1 min of dermabrasion and image acquisition (t = 1 min, Figure 1a), one of OCA mixtures (~100 μL) was topically applied, and skin was exposed to therapeutic ultrasound twice for 5 min duration each (Figure 1b). Between and after ultrasound applications (t = 6 and 11 min, respectively),

TABLE 1 | Nine mixtures of OCA and CPE with corresponding compound concentrations (%, v/v) that meet the FDA-allowed concentration threshold.

OCA number	OCA compound, concentration (%, v/v)	CPE compound, concentration (%, v/v)	Distilled water, concentration (%, v/v)
1	PEG (3.52)	OA (7.44%) + PG (89.04%)	
2	PEG (3.52)	PG (92.48%)	
3	PEG (3.52)	DMSO (45.5%) + PG (50.98%)	
4	Glucose (50)	OA (7.44%) + PG (42.56%)	
5	Glucose (50)	PG (50%)	
6	Glucose (50)	DMSO (45.5%)	4.5
7	Sucrose (50)	OA (7.44%) + PG (42.56%)	
8	Sucrose (50)	PG (50%)	
9	Sucrose (50)	DMSO (45.5%)	4.5

FIGURE 1 | Experimental in vivo human skin sites at different optical clearing experimental steps: (a) 1 min of dermabrasion, (b) skin with topically applied OCA exposed twice to 5 min of sonophoresis, (c) LC-OCT image acquisition during the entire experimental protocol.

as well as for 30 min with 5 min intervals after manipulations were over (Figure 1c), LC-OCT imaging was performed ($t = 16$, 21, 26, 31, 36, and 41 min). Small amount of corresponding OCA was placed between the skin and the probe glass plate during image acquisitions to minimize reflections at the interface.

Control measurements were conducted at similar time points ($t = 0$ to 41 min) on the same skin site only subjected to paraffin oil as the LC-OCT probe immersion liquid (neither dermabrasion nor ultrasound was applied).

2.5 | Processing of LC-OCT Images to Estimate μ_s and g From Skin Layers In Vivo

2.5.1 | Theoretical Background of the Model

More detailed explanation of the model proposed by Jacques et al. and later adapted for LC-OCT imaging system by Waszczuk et al. can be found in [13, 16]. To estimate the OPs of scattering media considering multiple forward scattering, the following modified exponential decay model of the depth-resolved reflectance $R(z)$, as proposed by Jacques et al. [13], was implemented:

$$R(z) = \rho\, exp^{-2\mu_{eff}z}, \tag{2}$$

with

$$\begin{cases} \mu_{eff} = G(g, \mathrm{NA})\left(\mu_a + a(g)\mu_s\right) \\ \rho = \mu_s \Delta Z b(g, \mathrm{NA}) \end{cases}, \tag{3}$$

where ρ is the fraction of the light backscattered from the focus into the collection angle of the LC-OCT objective; $\mu_a(\lambda)$, $\mu_s(\lambda)$, and $g(\lambda)$ are the absorption, scattering, and anisotropy coefficients; NA is the numerical aperture; ΔZ is the axial resolution of the imaging system; and $G(g, \mathrm{NA})$, $a(g)$, and $b(g, \mathrm{NA})$ are the model parameters described in [13]. $G(g, \mathrm{NA})$ takes into account the average photon path length considering the NA of the imaging system and the anisotropy factor g of the sample. For the LC-OCT setup used in this study, G was set to 1 (for NA = 0.5) [13]. $a(g)$ reflects the possibility of photon to reach the focus in highly forward scattering media despite multiple scattering. For cases of isotropic scattering, $a(g)$ is close to 1, while for highly forward scattering medium $a(g)$ tends forward 0. This parameter describes the slowed-down attenuation of light with depth by the so-called "serpentile phantoms" [16]. $0 \le b(g, \mathrm{NA}) \le 1$ is the fraction of light that is scattered within the focus in such a way that it can be collected by the LC-OCT objective lens. It is ruled by the phase function of the sample and the numerical aperture of the imaging system [13]. The factor 2 in Equation (2) accounts for the round-trip light attenuation by the sample. Since scattering in most biological tissue dominates over absorption ($\mu_s >> \mu_a$), the role of absorption was neglected in this study [9].

2.5.2 | Image Processing Algorithm to Estimate μ_s and g Values

The model described above assumed μ_{eff} and ρ parameters as the experimental observables. Thus, to deduce OPs (at the central wavelength $\lambda = 800$ nm of LC-OCT imaging system) $\mu_s(\lambda_{800})$ and $g(\lambda_{800})$, the observables must be extracted from 3D LC-OCT images and then mapped to the model described by Equations (2) and (3). To do that, a mean intensity profile $I(z)$ (of a 0.8 mm × 0.3 mm ($x \times y$) central part of each individual horizontal section) over depth z of a 3D LC-OCT image (Figure 2) was calculated and then converted into reflectance $R(z)$ using relation $fI(z) = R(z)$. Calibration constant f can be obtained using double integrating sphere measurements on a calibration phantom [13]. In this work, the calibration phantom with known OPs (estimated by the integrating spheres measurement as 4.6 mm^{-1} and 0.68 for μ_s and g, respectively) was kindly provided by Lena Waszczuk et al. [16].

Then, a linear regression fit was applied separately to two parts of the intensity profile, corresponding to the epidermal and dermal layers (Figure 2b). Fitting areas were delineated manually for each layer, considering mostly linear parts of attenuation slope before the background of multiply scattered light becomes dominant and changes the slope [13]. μ_{eff} parameter of each layer (μ_{eff}^{epi} for epidermis and μ_{eff}^{der} for dermis) was calculated as half of each linear fit slope. Epidermal ρ^{epi} parameter corresponding to the intercept of epidermal linear fit with depth $z = 0$, which is the interface between the LC-OCT probe glass surface and the skin surface. For the dermis, ρ^{der} was obtained from $\rho^{der} e^{-2\mu_{eff}^{epi}\delta z}$ (i.e., an intercept with between layer interface—basal membrane) by dividing it by the correction factor $e^{-2\mu_{eff}^{epi}\delta z}$ (or by multiplying it with correction factor $e^{2\mu_{eff}^{epi}\delta z}$) to compensate the attenuation by the epidermal layer of thickness δz (Figure 2b).

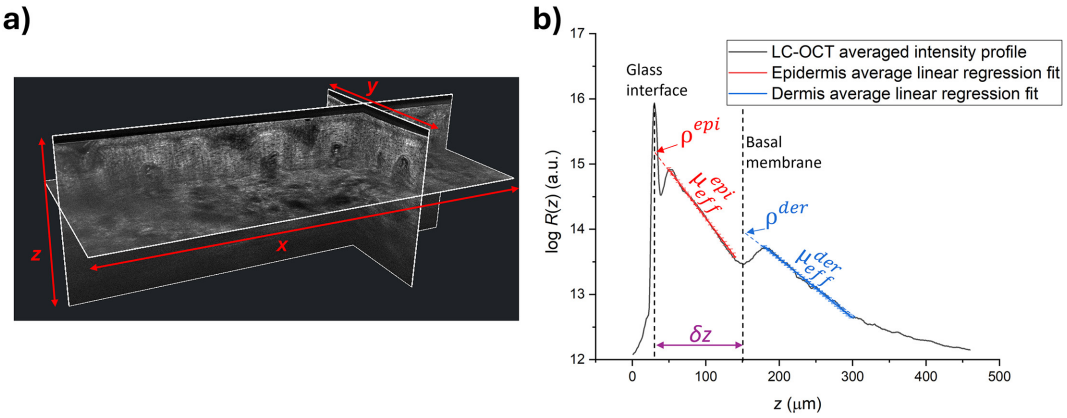

FIGURE 2 | (a) 3D LC-OCT image of human skin in vivo, represented in slice view and (b) averaged intensity profile $R(z)$, showing mean linear regression fit of each skin layer (epidermis—red, dermis—blue) and a corresponding pair of observables (ρ^{epi}, μ_{eff}^{epi} and ρ^{der}, μ_{eff}^{der}). Dermal layer parameter ρ^{der} deduced from the intercept with basal membrane ($z = \sim 150\,\mu m$) and corrected from epidermal layer attenuation.

Resulting experimental observables of each layer were then mapped to the model, described by Equations (2) and (3), using the following expression proposed by Jacques et al., considering $\mu_s >> \mu_a$: [13]

$$\frac{\mu_{eff}}{\rho} = \frac{aG}{b\Delta z} \tag{4}$$

Such expression has the advantage of being independent of μ_s and depends only on wavelength, NA, and g. With our experimental values $\lambda = 800\,nm$ and NA = 0.5, the anisotropy factor g of the corresponding layer was then retrieved as a function of μ_{eff}/ρ (as demonstrated in the works of Jacques and Waszczuk) [13, 16]. After retrieving $g(\lambda_{800})$ parameter, $\mu_s(\lambda_{800})$ parameter can be calculated using Equations (2) and (3).

For each 3D image, a linear fit of each layer was repeated more than 100 times by scanning the fit limits by 10 μm with 1 μm step to estimate the variability of the fitting depending on the range chosen. Then, resulting kinetic changes of those parameters (in %) were averaged among volunteers with respect to timepoint of measurement and OCA mixture applied. This was done to make the observed changes more consistent, as the initial values (intact skin measurements) are different between the volunteers due to interpatient variability.

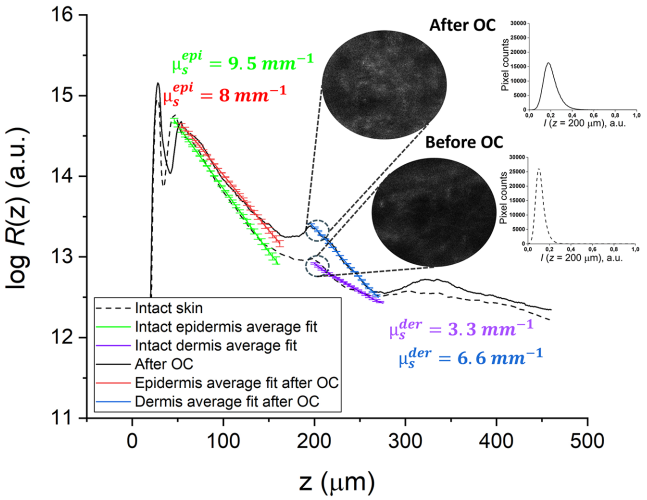

FIGURE 3 | Averaged skin LC-OCT intensity profiles $R(z)$ as a function of depth of one volunteer before (black dashed line) and after (black solid line) OC with a mixture of polyethylene glycol, oleic acid, and propylene glycol with linear regression fit lines of epidermal and dermal layers and corresponding μ_s estimated values. Round insets display LC-OCT horizontal sections of dermal layer at 200 μm depth before ($t = 0\,min$) and after OC ($t = 11\,min$). The graphs next to the insets are the corresponding pixel intensity distributions.

3 | Results and Discussion

Scanning the manually established fit limits did not significantly affect the estimation of skin OPs. The scattering coefficient $\mu_s(\lambda_{800})$ mean standard deviation (SD) for all OCA and all timepoints was only ~5% and ~3% for epidermal and dermal layers, respectively. The same values for the anisotropy factor $g(\lambda_{800})$ were ~0.05% and ~5%. Thus, there was almost no influence of manual fitting range delineation on estimated OPs.

Figure 3 shows the average of two LC-OCT intensity profiles $R(z)$ before and after OC, together with the corresponding linear regression fits of the epidermal and dermal layers with the corresponding μ_s values. It can be seen from the round insets and the corresponding pixel intensity distributions that the image contrast and brightness from the dermal layer (at 200 μm depth) are increased after optical clearing.

In order to illustrate the effect of skin optical clearing visible on OCT images, an example of cross-sectional views (B-scans extracted from 3D LC-OCT images) of the same skin area of one volunteer before and after treatment with the PEG/OA/PG mixture is presented in Figure 4a,b, respectively. The increase in image intensity and contrast is clearly visible above and below the dermoepidermal junction (DEJ, red dashed lines in Figure 4). In Figure 4a, the dermis layer of the skin before OCA application mostly appears as a low-contrast dark area while, in Figure 4b, bright structures (such as collagen bundles) can be distinguished throughout the entire visualized depth after optical clearing. Moreover, the surface reflectivity from the SC

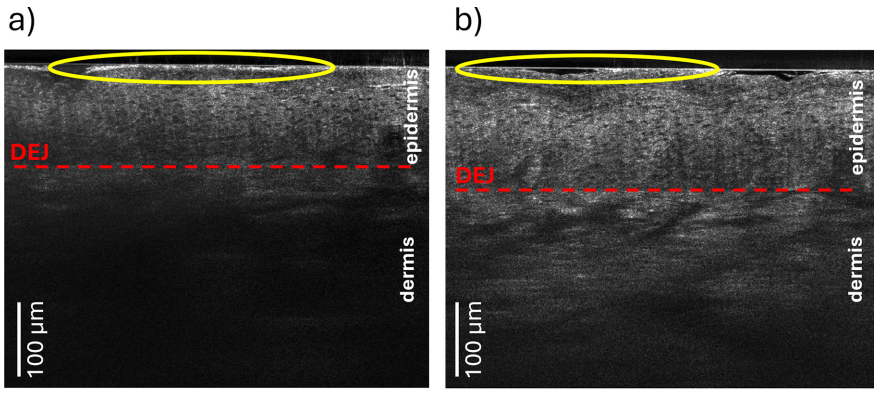

FIGURE 4 | Cross-sectional views (B-scans extracted from 3D LC-OCT images) of the same skin area of one volunteer before (a) and after (b) optical clearing with the mixture PEG/OA/PG (OA—oleic acid; PG—propylene glycol; PEG—polyethylene glycol) showing the increase in image intensity and contrast clearly visible above and below the dermoepidermal junction (DEJ, red dashed lines). The yellow ovals show the superficial area represented by the SC layer whose reflectivity has decreased after OC.

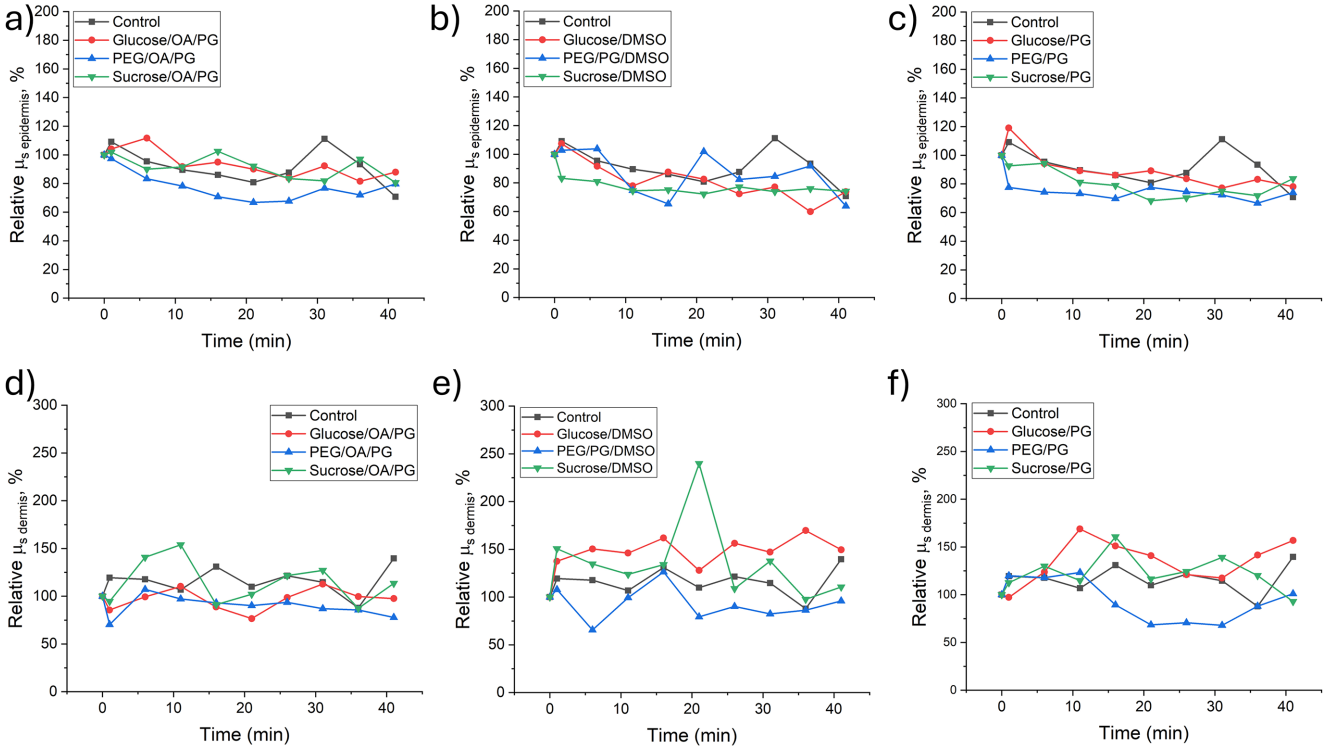

FIGURE 5 | Relative changes (expressed as % of intact skin value) of epidermal (a–c) and dermal (d–f) average ($n = 3$) scattering coefficient μ_s^{epi} and μ_s^{der}, caused by the in vivo skin optical clearing protocol as a function of time (OA—oleic acid; PG—propylene glycol; PEG—polyethylene glycol; DMSO—dimethyl sulfoxide). Standard deviation bars were removed to keep data legible.

layer (yellow ovals in Figure 4) decreased after OC. The area of the lower epidermis above the DEJ also became slightly brighter after optical clearing.

Relative changes (in % of intact skin value) of scattering coefficients μ_s^{epi} and μ_s^{der} (of epidermal and dermal layers, respectively) for the nine OCA and a control condition as a function of time are presented in Figure 5. Similar results, but for epidermal/dermal anisotropy factor $g^{epidermis}$ and g^{dermis}, are presented in Figure 6. SD bars that represent the variation between three volunteers were removed from the graphs for the sake of clarity (due to strong overlapping between bars) and presented separately in Table 2 (mean values over 10 timepoints) with respect to OP, layer, and OCA used.

Most of the curves related to the dermis OPs show high standard deviation bars that are overlapped for the consecutive values (unlike the epidermis), thus hardening the interpretation of the observable kinetic changes (Figures 5 and 6d–f) (Table 2). This is possibly due to the combined effect of measurement uncertainties propagated through the Jacques model. Additional reason might be the unstable LC-OCT probe positioning, which was constantly reapplied to tested skin sites without the possibility to use any kind of adhesive position-tracking labels due to

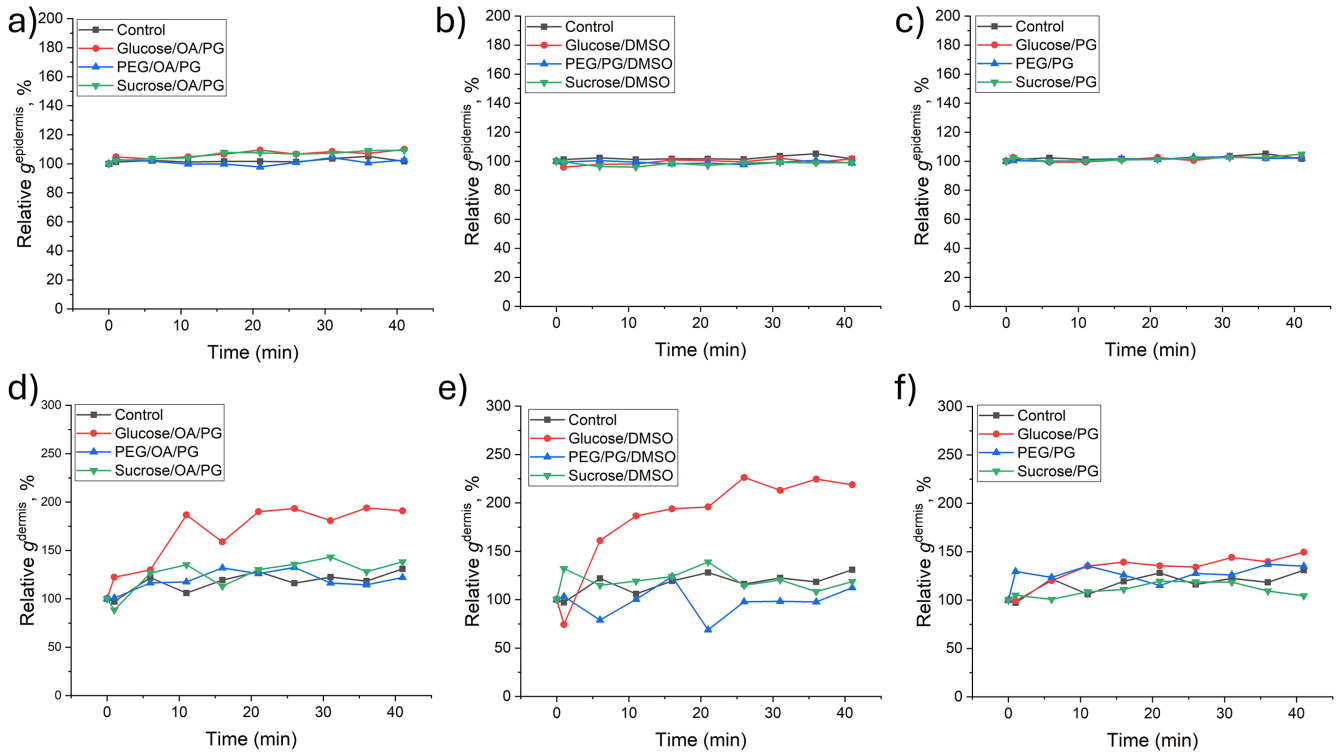

FIGURE 6 | Relative changes (expressed as % of intact skin value) of epidermal (a–c) and dermal (d–f) average ($n = 3$) anisotropy factor $g^{epidermis}$ and g^{dermis}, caused by the in vivo skin optical clearing protocol as a function of time (OA—oleic acid; PG—propylene glycol; PEG—polyethylene glycol; DMSO—dimethyl sulfoxide). Standard deviation bars were removed to keep data legible.

TABLE 2 | Mean standard deviation (SD, expressed as % of data) over 10 experimental time points representing the variation between three volunteers with respect to the estimated optical property, skin layer, and OCA used.

OCA mixture	SD of μ_s^{epi} (%)	SD of $g^{epidermis}$ (%)	SD of μ_s^{der} (%)	SD of g^{dermis} (%)
Control	25	3	24	30
PEG/OA/PG	9	6	26	21
PEG/PG	10	3	32	29
PEG/PG/DMSO	15	3	41	18
Glucose/OA/PG	11	6	16	81
Glucose/PG	11	5	24	40
Glucose/DMSO	10	2	50	123
Sucrose/OA/PG	22	5	43	41
Sucrose/PG	10	5	64	11
Sucrose/DMSO	12	1	42	22

mechanical manipulations with the skin surface at the beginning of the experimental protocol, making it impossible to analyze exactly the same tissue volume throughout the experiment. Another reason might be the morphological variation between the dermal layers of the volunteers and a more significant contribution of multiple scattering to the dermal layer linear fit (as compared to epidermis) [16].

The uncertainties mentioned in the previous paragraph are described in detail in the work of Waszczuk et al. [16] First, there are uncertainties on the OPs, estimated for a calibration phantom using double integrating spheres, which are then used in LC-OCT image processing. Second, there is an effect of both linear fit accuracy and variation between different images of the same sample on the μ_{eff} and ρ parameters. Finally, all these uncertainties affect the resulting LC-OCT estimation of scattering coefficient and anisotropy factor. However, despite it was mentioned by Waszczuk et al. that when propagating through the model of Jacques, the errors were amplified for high values of $\mu_s(\lambda_{800})$ and $g(\lambda_{800})$. This method is still well suited to samples

with relatively high anisotropy ($g(\lambda_{800})$ factor ranged between 0.7 and 0.9) and scattering coefficients $\mu_s(\lambda_{800})$ up to 12 mm^{-1}, that is, biological tissues such as skin.

Epidermis scattering coefficient demonstrated ~20% decrease for the control condition. But with a mean standard deviation over time of 25% of the observed values (Table 2) and the significant overlapping, it can be concluded that control conditions in general do not significantly affect the skin OPs. However, it can also be seen that some OCA caused noticeable clearing effect in the dermis. For example, a mixture of both sugars with DMSO caused a decrease in epidermis scattering μ_s^{epi} (Figure 5b). Sucrose/DMSO mixture effect resulted in 28% ± 18% decrease after 21 min of experimental protocol. Such a decrease overcomes a moderate overall standard deviation (mean ~12% for all timepoints). Mixture of glucose and DMSO demonstrated more pronounced effect—40% ± 3% of epidermal scattering decrease (from 8.3 ± 1.3 mm^{-1} to 5 ± 0.9 mm^{-1} for three volunteers), which is greater than the mean variation of data over the time for this OCA—10%. Both mixtures demonstrated an increase in anisotropy of a dermal layer as well. However, as mentioned above and can be seen in Table 2, dermis values have a relatively high standard deviation, making it onerous to conclude that there is a clearing effect on dermis. So, only the general behavior can be mentioned. The result for glucose/DMSO mixture is in a good agreement with observations made in our previous publication, where this mixture was considered as one of the most efficient among nine OCA in terms of in-depth increase of LC-OCT image intensity and contrast [26]. Such increase was assumed to be caused by the epidermis scattering decrease, which is quantitatively assessed in this study. Other notable results are related to the mixtures of glucose and PEG with PG as a permeation enhancer. Glucose/PG mixture (Figure 5c) caused a 23% decrease of epidermal scattering with the mean ~11% data variation over time and PEG/PG mixture caused a 33% decrease with ~10% mean data variation.

PEG/OA/PG mixture demonstrated the most pronounced μ_s^{epi} decrease (Figure 5a, blue triangle data points). Already after 21 min of experimental protocol (10 min after ultrasound-assisted clearing was over), this parameter decreased by 33% ± 17% for three volunteers, from 9.9 ± 1.1 mm^{-1} down to 6.6 ± 1.7 mm^{-1}. It can be seen that the decrease pattern in this case is the most confident among the other OCA. Moreover, for the first six measurement points (up to $t = 21$ min), the mean standard deviation is only ~5% of the data (overall SD is ~9% of the data). Considering all the mentioned uncertainties and high standard deviation bars in the case of other mixtures, PEG/OA/PG mixture demonstrated the most significant clearing effect. That is also in good agreement with previous observations [26], where PEG/OA/PG mixture demonstrated the best increase (40%) in image in-depth intensity and contrast after 10 min of ultrasound-assisted clearing.

Concerning the anisotropy parameter, none of the OCA demonstrated significant changes in $g^{epidermis}$ with relatively low SD values. Together with a decrease in μ_s^{epi}, one can conclude that OCA clearing effect on epidermis expressed and limited to matched RI of scattering particles and interstitial fluid. This RI matching effect is a well-investigated cause of the reduction in tissue scattering mentioned in the literature [17]. On the contrary, dermal scattering does not change significantly due to high SD, but the tendency of dermal anisotropy g^{dermis} toward increase indicates a different influence of tested OCA on skin dermis than to the epidermis in vivo. Mie theory explains that such behavior is related to an increase in the size of the scattering particles rather than to RI matching [19]. This applies to the dermis as there are bundles of collagen, which are probably swollen under the action of OCA mixtures, causing light to scatter in the forward direction. Applied to our results, we observed an increase in dermal anisotropy factor g^{dermis}, which might be linked to swelling of the dermal fibers considering Mie's theory, suggesting the OCA indeed penetrated into the dermal layer.

Our results obtained on in vivo human skin demonstrate the possibility of LC-OCT quantitative estimation of changes in skin scattering coefficient $\mu_s(\lambda_{800})$ and anisotropy factor $g(\lambda_{800})$, caused by biocompatible optical clearing (involving the reduced concentrations of clearing agents used together with chemical and physical permeation enhancers). Moreover, the mixture of PEG/OA/PG has shown the best results. Although our current results were not validated with integrating spheres measurements (as the study was carried out on skin in vivo), this was done on phantoms in the study of Waszczuk et al., demonstrating a good correlation between the values obtained using integrating spheres and application of Jacques' model to LC-OCT images [16]. The results obtained in this study allowed us to quantitatively assess the effect of biocompatible optical clearing on the scattering OPs of the skin (hypothesized in our previous study [26]), which subsequently leads to an increase in the in-depth intensity and contrast of LC-OCT images. In addition, despite the reduced concentrations of the OCA used, the proposed idea to combine them with dermabrasion and ultrasound nevertheless allows diffusion down to the dermis layer, which was confirmed in this study through an increase in the dermal anisotropy after optical clearing.

4 | Conclusion

In the present contribution, values of scattering coefficient and anisotropy factor (at 800 nm) of human skin epidermis and dermis layers were quantitatively estimated directly from in vivo LC-OCT images using a modified exponential decay model of the depth-resolved reflectance. Furthermore, the modifications of the values of these optical parameters were demonstrated following the topical application of different clinical use-compatible OCAs (combined with dermabrasion and ultrasound physical enhancements) on in vivo human skin. In the epidermis layer, optical clearing effect was mostly expressed in a decrease of the scattering coefficient value (−33% ± 17%), related to RI matching between scattering particles within the tissue and the interstitial fluid. In dermis layer, it was mostly observed as an increase of the anisotropy factor related to the swelling of the collagen fibers. Furthermore, reducing the concentration of OCAs to meet the threshold concentration requirements for clinical use may significantly affect the clearing efficiency. However, this could be compensated by combining dermabrasion and sonophoresis, as demonstrated in the current study.

Author Contributions

Sergey M. Zaytsev was involved in methodology, investigation, data processing and modeling, formal analysis, writing – original draft, review and editing. Léna Waszczuk was involved in data processing and modelling, writing – review and editing. Jonas Ogien was involved in writing – review and editing. Arnaud Dubois was involved in conceptualization, writing – review and editing, and project management. Walter Blondel and Marine Amouroux were involved in conceptualization, methodology, formal analysis, writing – review and editing, and project management. All authors have read and agreed to the published version of the manuscript.

Acknowledgments

This research was carried out with the support of the French National Research Agency (ANR) under the French PIA project "Lorraine Université d'Excellence" (ANR-15-IDEX-04-LUE). This study was part of the Spec-LCOCT project funded by the ANR (ANR-21-CE19-0056) and was carried with the DeepLive device of the PhotoVivo platform, which is part of the France Life Imaging (FLI) network and funded by Contrat de Plan Etat-Région Grand Est 2015-2020 (CPER IT2MP: Innovations Technologiques, Modélisation et Médecine Personnalisée) thanks to the financial support by European Regional Development Fund (FEDER), Grand Est Region and Ligue Contre le Cancer.

Conflicts of Interest

The authors declare no conflicts of interest.

Data Availability Statement

The data that support the findings of this study are available from the corresponding author upon reasonable request.

References

1. T. B. Fitzpatrick, *Dermatology in General Medicine* (New York: Mcgraw-Hill Book Co, 1993).

2. V. Narayanamurthy, P. Padmapriya, A. Noorasafrin, et al., "Skin Cancer Detection Using Non-Invasive Techniques," *RSC Advances* 8, no. 49 (2018): 28095–28130, https://doi.org/10.1039/C8RA04164D.

3. V. V. Tuchin, J. Popp, and V. Zakharov, *Multimodal Optical Diagnostics of Cancer*, 1st ed. (Cham: Springer, 2020).

4. J. Ogien, A. Daures, M. Cazalas, J. L. Perrot, and A. Dubois, "Line-Field Confocal Optical Coherence Tomography for Three-Dimensional Skin Imaging," *Frontiers of Optoelectronics* 13, no. 4 (2020): 381–392, https://doi.org/10.1007/s12200-020-1096-x.

5. A. Dubois, O. Levecq, H. Azimani, et al., "Line-Field Confocal Time-Domain Optical Coherence Tomography With Dynamic Focusing," *Optics Express* 26, no. 26 (2018): 33534–33542, https://doi.org/10.1364/OE.26.033534.

6. F. Latriglia, J. Ogien, C. Tavernier, et al., "Line-Field Confocal Optical Coherence Tomography (LC-OCT) for Skin Imaging in Dermatology," *Lifestyles* 13, no. 12 (2023): 2268, https://doi.org/10.3390/life13122268.

7. M. Suppa, M. Fontaine, G. Dejonckheere, et al., "Line-Field Confocal Optical Coherence Tomography of Basal Cell Carcinoma: A Descriptive Study," *Journal of the European Academy of Dermatology and Venereology* 35, no. 5 (2021): 1099–1110, https://doi.org/10.1111/jdv.17078.

8. C. Ruini, S. Schuh, E. Sattler, and J. Welzel, "Line-Field Confocal Optical Coherence Tomography—Practical Applications in Dermatology and Comparison With Established Imaging Methods," *Skin Research and Technology* 27, no. 3 (2021): 340–352, https://doi.org/10.1111/srt.12949.

9. V. V. Tuchin, *Tissue Optics: Light Scattering Methods and Instruments for Medical Diagnosis*, 3rd ed. (Bellingham: SPIE Press, 2015), https://doi.org/10.1117/3.1003040.

10. S. Chang and A. K. Bowden, "Review of Methods and Applications of Attenuation Coefficient Measurements With Optical Coherence Tomography," *Journal of Biomedical Optics* 24, no. 9 (2019): 090901, https://doi.org/10.1117/1.JBO.24.9.090901.

11. L. Thrane, H. T. Yura, and P. E. Andersen, "Analysis of Optical Coherence Tomography Systems Based on the Extended Huygens-Fresnel Principle," *Journal of the Optical Society of America. A, Optics, Image Science, and Vision* 17, no. 3 (2000): 484–490, https://doi.org/10.1364/josaa.17.000484.

12. L. Thrane, M. H. Frosz, T. M. Jørgensen, A. Tycho, H. T. Yura, and P. E. Andersen, "Extraction of Optical Scattering Parameters and Attenuation Compensation in Optical Coherence Tomography Images of Multilayered Tissue Structures," *Optics Letters* 29, no. 14 (2004): 1641–1643, https://doi.org/10.1364/OL.29.001641.

13. S. L. Jacques, "Confocal Laser Scanning Microscopy Using Scattering as the Contrast Mechanism," in *Handbook of Coherent-Domain Optical Methods: Biomedical Diagnostics, Environmental Monitoring, and Materials Science*, ed. V. V. Tuchin (NY: Springer, New York, 2013), 1157–1170, https://doi.org/10.1007/978-1-4614-5176-1_28.

14. R. Samatham and S. L. Jacques, "Determine Scattering Coefficient and Anisotropy of Scattering of Tissue Phantoms Using Reflectance-Mode Confocal Microscopy," *Proceedings of SPIE* 7187 (2009): 152–159, https://doi.org/10.1117/12.809684.

15. N. Choudhury and S. L. Jacques, "Extracting Scattering Coefficient and Anisotropy Factor of Tissue Using Optical Coherence Tomography," *Proceedings of SPIE–The International Society for Optical Engineering* 8221 (2012): 144–148, https://doi.org/10.1117/12.907401.

16. L. Waszczuk, J. Ogien, F. Pain, and A. Dubois, "Determination of Scattering Coefficient and Scattering Anisotropy Factor of Tissue-Mimicking Phantoms Using Line-Field Confocal Optical Coherence Tomography (LC-OCT)," *Journal of the European Optical Society-Rapid Publications* 19, no. 2 (2023): 2, https://doi.org/10.1051/jeos/2023037.

17. V. V. Tuchin, D. Zhu, and E. A. Genina, *Handbook of Tissue Optical Clearing: New Prospects in Optical Imaging*, 1st ed. (Boca Raton: Routledge & CRC Press, 2022), https://doi.org/10.1201/9781003025252.

18. L. M. C. Oliveira and V. V. Tuchin, "Optical Clearing and Tissue Imaging," in *The Optical Clearing Method: A New Tool for Clinical Practice and Biomedical Engineering*, eds. L. M. C. Oliveira and V. V. Tuchin (Cham: Springer, 2019), 107–138, https://doi.org/10.1007/978-3-030-33055-2_7.

19. R. Samatham, K. G. Phillips, and S. L. Jacques, "Assessment of Optical Clearing Agents Using Reflectance-Mode Confocal Scanning Laser Microscopy," *Journal of Innovative Optical Health Sciences* 3, no. 3 (2010): 183–188, https://doi.org/10.1142/S1793545810001064.

20. G. Vargas, A. Readinger, S. S. Dozier, and A. J. Welch, "Morphological Changes in Blood Vessels Produced by Hyperosmotic Agents and Measured by Optical Coherence Tomography," *Photochemistry and Photobiology* 77, no. 5 (2003): 541–549, https://doi.org/10.1562/0031-8655(2003)0770541MCIBVP2.0.CO2.

21. V. V. Tuchin, A. N. Bashkatov, E. A. Genina, Y. P. Sinichkin, and N. A. Lakodina, "In Vivo Investigation of the Immersion-Liquid-Induced Human Skin Clearing Dynamics," *Technical Physics Letters* 27, no. 6 (2001): 489–490, https://doi.org/10.1134/1.1383834.

22. "U. S. Food and Drug Administration, Inactive Ingredients Database, FDA.Government," (2019), https://www.accessdata.fda.gov/scripts/cder/iig/index.cfm.

23. Z. Zhi, Z. Han, Q. Luo, and D. Zhu, "Improve Optical Clearing of Skin In Vitro With Propylene Glycol as a Penetration Enhancer," *Journal of Innovative Optical Health Sciences* 2, no. 3 (2009): 269–278, https://doi.org/10.1142/S1793545809000590.

24. Y. Liu, X. Yang, D. Zhu, R. Shi, and Q. Luo, "Optical Clearing Agents Improve Photoacoustic Imaging in the Optical Diffusive Regime," *Optics Letters* 38, no. 20 (2013): 4236–4239, https://doi.org/10.1364/OL.38.004236.

25. E. A. Genina, Y. I. Surkov, I. A. Serebryakova, A. N. Bashkatov, V. V. Tuchin, and V. P. Zharov, "Rapid Ultrasound Optical Clearing of Human Light and Dark Skin," *IEEE Transactions on Medical Imaging* 39, no. 10 (2020): 3198–3206, https://doi.org/10.1109/TMI.2020.2989079.

26. S. M. Zaytsev, M. Amouroux, V. V. Tuchin, E. A. Genina, and W. Blondel, "In Vivo Skin Optical Clearing Efficacy Quantification of Clinically Compatible Agents Using Line-Field Confocal Optical Coherence Tomography," *Journal of Biomedical Optics* 28, no. 5 (2023): 055002, https://doi.org/10.1117/1.JBO.28.5.055002.

27. N. Sudheendran, M. Mohamed, M. G. Ghosn, V. V. Tuchin, and K. V. Larin, "Assessment of Tissue Optical Clearing as a Function of Glucose Concentration Using Optical Coherence Tomography," *Journal of Innovative Optical Health Sciences* 3, no. 3 (2010): 169–176, https://doi.org/10.1142/S1793545810001039.

28. J. Ogien, C. Tavernier, S. Fischman, and A. Dubois, "Line-Field Confocal Optical Coherence Tomography (LC-OCT): Principles and Practical Use," *Italian Journal of Dermatology and Venereology* 158, no. 3 (2023): 171–179, https://doi.org/10.23736/S2784-8671.23.07613-2.